NOZZLE FLOW COMPUTATIONS USING THE EULER EQUATIONS

João L.F. Azevedo, Nide G.C.R. Fico Jr.
Instituto de Aeronáutica e Espaço
Centro Técnico Aeroespacial
12225 São José dos Campos SP — BRASIL

Marcos A. Ortega, Guilherme C. Luna
Instituto Tecnológico de Aeronáutica
Centro Técnico Aeroespacial
12225 São José dos Campos SP — BRASIL

Abstract

Inviscid, transonic, convergent-divergent nozzle flowfields are simulated using the Beam and Warming implicit approximate factorization algorithm. Both two-dimensional and axisymmetric nozzle configurations are considered. Nonlinear artificial dissipation terms are explicitly added, and variable time stepping is used for steady state convergence acceleration. A procedure for using one-dimensional characteristic relations for boundary condition enforcement in the axisymmetric case was developed and implemented. Studies of several numerical boundary condition effects on solution accuracy and convergence rate were performed. The algorithm proved to be very robust, and solutions on rather realistic nozzle configurations were obtained. Present computational results show good agreement with the available data. The algorithm with the variable time stepping option proved to be computationally efficient.

Introduction

Nozzle flows play an important role in many aerospace applications. However, experiments that can duplicate the actual operating environment of these nozzles can be rather costly, or even impractical. Hence, it is of great interest to seek to develop computational procedures that could accurately, and efficiently, simulate the flowfield in such devices. Moreover, it is significant that not only the propulsion system performance is affected by the nozzle flow, but also the external aerodynamics and aerothermodynamics of the vehicle can be influenced by it, especially close to the base region.

The present work reports on the efforts for the development of efficient and robust two-dimensional and axisymmetric Euler solvers for inlet and nozzle flow applications. The governing equations are written in strong conservation-law form for general body conforming curvilinear coordinates. The equations are solved using the Beam and Warming implicit approximate factorization algorithm[1, 2, 3], in which the implicit Euler method is used for the time march and central differences are employed to discretize all spatial derivatives. As usual with the Beam and Warming scheme, artificial dissipation terms have to be added in order to control nonlinear instabilities. Here, both a linear constant coefficient model[3] and Pulliam's nonlinear model[4, 5, 6] were implemented. Boundary conditions were implemented explicitly in the present work. Symmetry conditions are used at the centerline, flow tangency is considered at the nozzle wall, and the entrance and exit conditions are based on the concept of one-dimensional characteristic relations for the 2-D Euler equations[7, 8].

The ultimate goal of the research work here described would be to develop the capability of simulating realistic solid rocket motor nozzle flows. To this end, the following aspects were systematically studied and are presented here: (1) influence of the magnitude of the artificial dissipation coefficients and of the type of model in the solution; (2) implementation of numerical boundary conditions and their overall effect on the accuracy and robustness of the code; (3) consideration of realistic nozzle geometries and their effect on the capability of the code to handle large convergent/divergent section angles and small throat radii. Moreover, systematic grid refinement studies were performed aimed at a thorough code validation and assessment of numerical accuracy.

Two-Dimensional Formulation

The Euler equations can be written in conservation-law form for a body-conforming, 2-D, curvilinear coordinate system as

$$\frac{\partial \overline{Q}}{\partial \tau} + \frac{\partial \overline{E}}{\partial \xi} + \frac{\partial \overline{F}}{\partial \eta} = 0 \qquad (1)$$

The vector of conserved quantities is

$$\overline{Q} = J^{-1} \begin{bmatrix} \rho & \rho u & \rho v & e \end{bmatrix}^T \qquad (2)$$

The inviscid flux vectors are given by

$$\overline{E} = J^{-1} \left\{ \begin{array}{c} \rho U \\ \rho u U + p\xi_x \\ \rho v U + p\xi_y \\ (e+p)U - p\xi_t \end{array} \right\} \qquad \overline{F} = J^{-1} \left\{ \begin{array}{c} \rho V \\ \rho u V + p\eta_x \\ \rho v V + p\eta_y \\ (e+p)V - p\eta_t \end{array} \right\} \qquad (3)$$

The usual nomenclature is being used here, such that ρ is the density, u and v are cartesian velocity components, and e is the total energy per unit of volume. Moreover, it is assumed in the above that a suitable nondimensionalization of the governing equations was performed. For instance, for the internal flow cases considered here, the density is referred to the entrance stagnation density (ρ_t), velocity components are normalized by the entrance critical speed of sound (a_*), and the total energy per unit of volume is referred to $\rho_t a_*^2$.

The pressure, p, is obtained from the equation of state for perfect gases, which can be written for the present purposes as

$$p = (\gamma - 1)\left[e - \frac{1}{2}\rho\left(u^2 + v^2\right)\right] \qquad (4)$$

The contravariant velocity components can be written as

$$\begin{aligned} U &= \xi_t + \xi_x u + \xi_y v \\ V &= \eta_t + \eta_x u + \eta_y v \end{aligned} \qquad (5)$$

The Jacobian of the transformation is given by

$$J = \left(x_\xi y_\eta - x_\eta y_\xi\right)^{-1} \qquad (6)$$

and the various metric terms can be expressed as

$$\begin{array}{ll} \xi_x = J y_\eta & \eta_x = -J y_\xi \\ \xi_y = -J x_\eta & \eta_y = J x_\xi \\ \xi_t = -x_\tau \xi_x - y_\tau \xi_y & \eta_t = -x_\tau \eta_x - y_\tau \eta_y \end{array} \qquad (7)$$

The subject of enforcing numerical boundary conditions has received special attention in the present work. It can be shown, using simple model equations, that improper "extrapolation rules" can even lead to numerical instability of the overall scheme. Here, the implementation of numerical boundary conditions was based on the one-dimensional characteristic relations of the inviscid gasdynamic equations. The basic concept is that the Euler equations can be diagonalized by a similarity transformation[9]. With this diagonalization, one-dimensional characteristic relations can be derived which represent the propagation of flow information along the characteristic lines (see, for example, MacCormack[7] and Roe[10]). From the local slope of the characteristics, it is possible to determine how many conditions should be specified at a given boundary and how many should be extrapolated from interior information. This is important to guarantee the well-posedness of the initial boundary value problem. For those conditions that must be extrapolated, the suggestion[7] is to use again the characteristic relations instead of some arbitrary extrapolation rule. The former carries some physics of the phenomena into the extrapolation process and, therefore, should provide for a more robust way of enforcing the numerical boundary conditions. The particular characteristic relation that should be used in each case is the one associated with the characteristic speed that is carrying information from the interior to the boundary.

The one-dimensional characteristic relations could be derived for a general curvilinear coordinate system. However, they are usually found in the literature for a Cartesian system. It must be emphasized that, at the boundaries where we might be interested in using these relations, the curvilinear and Cartesian coordinates are essen-

tially aligned. Moreover, the use of the relations in Cartesian coordinates has the objective of simplifying their numerical implementation. The formulation used here can be found in MacCormack[7], and the one-dimensional characteristic relations associated with "operation" in the x-direction for a two-dimensional flow can be written as

$$
\begin{aligned}
\frac{\partial \rho}{\partial t} - \frac{1}{a^2}\frac{\partial p}{\partial t} &= -u\left(\frac{\partial \rho}{\partial x} - \frac{1}{a^2}\frac{\partial p}{\partial x}\right) \\
\frac{\partial v}{\partial t} &= -u\frac{\partial v}{\partial x} \\
\frac{\partial p}{\partial t} + \rho a\frac{\partial u}{\partial t} &= -(u+a)\left(\frac{\partial p}{\partial x} + \rho a\frac{\partial u}{\partial x}\right) \\
\frac{\partial p}{\partial t} - \rho a\frac{\partial u}{\partial t} &= -(u-a)\left(\frac{\partial p}{\partial x} - \rho a\frac{\partial u}{\partial x}\right)
\end{aligned} \qquad (8)
$$

These are derived by assuming that flow changes in a specific "operating" direction are large when compared with changes in the other direction. This will allow the elimination, in the above case, of the y-derivatives in the Euler equations. Hence, we are still left with 4 conservation equations, but only spatial fluxes in the x-direction. These equations can, then, be diagonalized by premultiplication by the left eigenvector matrix of the corresponding inviscid flux Jacobian matrix, as described by Warming et al.[9]. In the above, a is the speed of sound, and it is interesting to observe that u, u, $u+a$ and $u-a$ are the eigenvalues of the inviscid flux Jacobian matrix associated with the Cartesian flux vector E. Similar expressions could be derived for "operation" in the y-direction, but those will not be necessary in our case.

For all cases treated in the present work, subsonic nozzle entrance conditions were considered. Hence, according to the characteristic relation analysis previously described, three conditions must be specified at the entrance and one must be obtained from extrapolation of interior information. We consider that the stagnation pressure, stagnation temperature and flow entrance angle are fixed at the entrance[11]. Since $u-a$ is the characteristic speed bringing information from the interior to the boundary, the fourth relation in the set of Eqs. (8) is used to obtain the remaining condition at the entrance boundary. A similar reasoning should be made at an exit station, except that one must consider both the possibilities of subsonic and supersonic exit. Although the conditions intended here will always result in a supersonic exit after convergence, the solution process is started by assuming stagnation conditions everywhere in the nozzle, except for the pressure difference at the exit which will drive the solution to convergence. For a subsonic exit, the exit static pressure is assumed fixed. The other three conditions at the exit are obtained by extrapolation of interior information using the first three relations of the set of Eqs. (8), which are the ones associated with the characteristic speeds that carry information from the interior to the boundary. All four relations of Eqs. (8) are used to obtain the properties at the exit in the supersonic case.

The other boundary conditions used consider flow tangency at nozzle walls and symmetry conditions at the nozzle centerline. For simplicity of implementation, we compute all conserved variables at a wall boundary. It is clear that, for an Euler formulation, it would be enough to compute the pressure at the wall and to impose that the convective flux in the wall-normal direction is zero. This would be the equivalent, in the present context, of Mavriplis'[12] weak boundary condition implementation. However, we have adopted a strong form of implementation[12] in which the properties themselves are defined at the wall boundary. Velocity components at the wall are obtained by extrapolating the U contravariant velocity component from the adjacent point and by imposing the tangency condition, i.e., $V = 0$ at the wall. The other properties at the wall were typically obtained by imposing a zero normal pressure gradient and a zero normal temperature gradient at the wall. We have also examined here the possibility of adding a centrifugal-type correction to the wall pressure boundary condition. From an analysis of the inviscid momentum equation in a direction normal to the wall (n), one finds that $(\partial p/\partial n) = 0$ is the correct pressure boundary condition for flat walls. For a convex wall, which typically is the case at a nozzle throat, some centrifugal influence should be taken into account. This can be done by setting

$$
\left(\frac{\partial p}{\partial n}\right)_{\text{wall}} = \frac{\rho\left(u^2 + v^2\right)}{R_{\text{wall}}} \qquad (9)
$$

where R_{wall} is the radius of curvature of the nozzle wall section considered.

In the 2-D case, the centerline boundary condition was implemented by assuming that an extra line of points existed on the other side of the centerline. Flow properties values at this extra line of points were determined by a reflection-type boundary condition, i.e., by flow symmetry considerations. This type of boundary condition enforcement is also equivalent to a strong boundary condition implementation in the sense discussed by Mavriplis[12]. Tests were also performed by implementing the centerline boundary condition in a weak fashion. In this case, the last line of mesh points is along the centerline itself, and the symmetry condition is enforced by imposing a zero convective flux across the centerline. The pressure at the centerline is obtained by zero-th order extrapolation of the pressure at the adjacent point. The final results are the same regardless of the form in which the centerline boundary condition is implemented.

Axisymmetric Formulation

The axisymmetric formulation implemented is very similar to the one presented by Nietubicz et al.[13]. This is actually an azimuthal invariant formulation, in which the Euler equations can be rewritten still in strong conservation-law form as

$$
\frac{\partial \overline{Q}}{\partial \tau} + \frac{\partial \overline{E}}{\partial \xi} + \frac{\partial \overline{F}}{\partial \eta} + \overline{H} = 0 \qquad (10)
$$

The vector of conserved variables, $\overline{Q}$, is given by Eq. (2), and the inviscid flux vectors, $\overline{E}$ and $\overline{F}$, are given by Eq. (3). The source term, $\overline{H}$, which arises in the axisymmetric case, can be written as[14]

$$
\overline{H} = J^{-1}\left[\begin{array}{cccc} 0 & 0 & -p/R & 0 \end{array}\right]^T \qquad (11)
$$

where $R = R(\xi, \eta, \tau)$ is the radial position in the natural inertial cylindrical coordinate system. We further observe that the axisymmetric equations given above are a simplification of the more general azimuthal invariant equations[13] for the case with no body rotation. The definition of the various terms that appear in the axisymmetric equations is exactly equal to the one used in the 2-D equations, except with regard to the Jacobian and the metric terms of the transformation. In the present case, the Jacobian of the transformation is given by[15, 16]

$$
J = \left[R\left(x_\xi y_\eta - x_\eta y_\xi\right)\right]^{-1} \qquad (12)
$$

and the various metric terms can be written as

$$
\begin{array}{ll}
\xi_x = JRy_\eta & \eta_x = -JRy_\xi \\
\xi_y = -JRx_\eta & \eta_y = JRx_\xi \\
\xi_t = -x_\tau\xi_x - y_\tau\xi_y & \eta_t = -x_\tau\eta_x - y_\tau\eta_y
\end{array} \qquad (13)
$$

Due to the term proportional to $1/R$ in the expression for the Jacobian, the centerline is a singularity of the transformation in the axisymmetric case.

Implementation of nozzle entrance and exit boundary conditions in the axisymmetric case has also used the concept of one-dimensional characteristic relations. Using assumptions similar to the ones adopted in the 2-D case, we can obtain the one-dimensional characteristic relations for "operation" in the x-direction for an axisymmetric flow as

$$
\begin{aligned}
\frac{\partial \rho}{\partial t} - \frac{1}{a^2}\frac{\partial p}{\partial t} &= -u\left(\frac{\partial \rho}{\partial x} - \frac{1}{a^2}\frac{\partial p}{\partial x}\right) \\
\frac{\partial v}{\partial t} &= -u\frac{\partial v}{\partial x} \\
\frac{\partial p}{\partial t} + \rho a\frac{\partial u}{\partial t} &= -(u+a)\left(\frac{\partial p}{\partial x} + \rho a\frac{\partial u}{\partial x}\right) - \frac{\gamma p v}{R} \\
\frac{\partial p}{\partial t} - \rho a\frac{\partial u}{\partial t} &= -(u-a)\left(\frac{\partial p}{\partial x} - \rho a\frac{\partial u}{\partial x}\right) - \frac{\gamma p v}{R}
\end{aligned} \qquad (14)
$$

We observe that the first two characteristic relations are not changed, with respect to their 2-D form, but the ones associated with the $(u+a)$ and $(u-a)$ eigenvalues do acquire a source term in the right-hand side.

At a subsonic entrance, we consider that the stagnation temperature, the stagnation pressure and the flow entrance angle are known. The fourth property at the entrance is obtained using the last relation of the set of Eqs. (14), which is the one associated with the character-

istic speed which brings information from the interior to the boundary. At a subsonic exit, the first three relations in the set of Eqs. (14) are used, together with a known value of exit static pressure, in order to determine the flow properties at the exit station. For a supersonic exit, all four characteristic relations are used in order to extrapolate the interior information to obtain the properties at the exit.

Property values at the nozzle wall are obtained from the flow tangency condition together with the assumption of zero normal pressure and temperature gradients, precisely in the same fashion as in the two-dimensional case. As previously discussed, this is the equivalent of a strong wall boundary condition implementation. In order to avoid the transformation singularity at the centerline, the boundary conditions at the nozzle axis of symmetry are implemented in the weak sense by simply imposing, in the residue computation, that the $\overline{F}$ flux vector at the centerline is identically zero. We emphasize that this is somewhat different from the condition used in the 2-D case, in which $V = 0$ at the centerline and, hence, the convective portion of the $\overline{F}$ flux is zero but the pressure term still survives. Here, in the axisymmetric case, aside from having $V = 0$, we also have that $J^{-1} = 0$. Therefore, $\overline{F} = 0$ at the centerline.

Numerical Algorithm

The governing equations, both in the 2-D and in the axisymmetric case, were discretized in a finite difference context using the Beam and Warming[1, 2, 3] algorithm. The time march is performed with the implicit Euler method in the present case, which yields first order accuracy in time. All spatial derivatives are discretized by three point, second order, centered finite difference expressions. The resulting left-hand side operators, after local linearization by Taylor series expansion, are approximately factored in the usual way with the Beam and Warming scheme. The resulting finite difference equations can be written, for the axisymmetric case, as

$$L_\xi L_\eta \Delta_t \overline{Q}^n = R_\xi + R_\eta - \Delta t \overline{H}^n \qquad (15)$$

The various operators are defined as

$$
\begin{aligned}
L_\xi &= I + \Delta t \, \delta_\xi \hat{A}^n - \Delta t \, \varepsilon_I J^{-1} \nabla_\xi \Delta_\xi J \\
L_\eta &= I + \Delta t \, \delta_\eta \hat{B}^n - \Delta t \, \varepsilon_I J^{-1} \nabla_\eta \Delta_\eta J \\
R_\xi &= -\Delta t \, \delta_\xi \overline{E}^n + D_\xi \\
R_\eta &= -\Delta t \, \delta_\eta \overline{F}^n + D_\eta
\end{aligned}
\qquad (16)
$$

In the above, δ_ξ and δ_η are central difference operators; ∇_ξ and ∇_η are backward difference operators; and Δ_ξ and Δ_η are forward difference operators in the ξ- and η-directions, respectively. The Δ_t is a forward difference operator in time defined as $\Delta_t \overline{Q}^n = \overline{Q}^{n+1} - \overline{Q}^n$. The inviscid flux Jacobian matrices $\hat{A}^n$ and $\hat{B}^n$, which appear in the local linearization process through Taylor series expansions, are described in detail by Pulliam[4], Pulliam and Steger[5] and Zdravistch[15], and their expressions will not be repeated here. The interested reader is referred to these references for the form of these matrices. Moreover, we observe that the source term was implemented explicitly in the present work. This approach was employed because the Jacobian matrix associated with the source term has only very few nonzero elements, and because previous experience with the present axisymmetric formulation[14, 15, 16] has shown that this approach does not cause any numerical instability problems. Finally, the finite difference equations which are obained in the 2-D case can be written in exactly the same form as Eq. (15), except that they do not contain the source term.

In the previous expressions, the artificial dissipation terms necessary for numerical stability of the algorithm have already been introduced. The Euler equations are a set of nondissipative hyperbolic equations and, hence, they require some form of numerical dissipation in order to damp high frequency uncoupled error modes and to prevent oscillations near shocks and other discontinuities[17]. Since the spatial derivatives are being approximated by central difference expressions, these artificial dissipation terms are not automatically provided by the spatial discretization scheme and they must be explicitly added. Here, both a constant coefficient artificial dissipation model[3] and a nonlinear model[4, 5, 6] have been implemented in the right-hand side operators. For the constant coefficient model, the D_ξ and D_η operators in Eqs. (16) are given by

$$
\begin{aligned}
D_\xi &= D_\xi^{(4)} = -\Delta t \, \varepsilon_E J^{-1} (\nabla_\xi \Delta_\xi)^2 J \overline{Q}^n \\
D_\eta &= D_\eta^{(4)} = -\Delta t \, \varepsilon_E J^{-1} (\nabla_\eta \Delta_\eta)^2 J \overline{Q}^n
\end{aligned}
\qquad (17)
$$

These are simply fourth difference terms, and the constant value of ε_E should be provided by the user. It is typically recommended in the literature that ε_E should be of order one. In this investigation, several tests were conducted varying the value of ε_E and these results will be presented later.

For the nonlinear model, the right-hand side artificial dissipation operators are given by[6]

$$
\begin{aligned}
D_{\xi_{i,j}} &= D_{\xi_{i,j}}^{(nl)} = \nabla_\xi \left(\sigma_{i+1,j} J_{i+1,j}^{-1} + \sigma_{i,j} J_{i,j}^{-1} \right) \\
&\qquad \left(\varepsilon_{\xi_{i,j}}^{(2)} \Delta_\xi J_{i,j} \overline{Q}_{i,j}^n - \varepsilon_{\xi_{i,j}}^{(4)} \Delta_\xi \nabla_\xi \Delta_\xi J_{i,j} \overline{Q}_{i,j}^n \right) \\
D_{\eta_{i,j}} &= D_{\eta_{i,j}}^{(nl)} = \nabla_\eta \left(\sigma_{i,j+1} J_{i,j+1}^{-1} + \sigma_{i,j} J_{i,j}^{-1} \right) \\
&\qquad \left(\varepsilon_{\eta_{i,j}}^{(2)} \Delta_\eta J_{i,j} \overline{Q}_{i,j}^n - \varepsilon_{\eta_{i,j}}^{(4)} \Delta_\eta \nabla_\eta \Delta_\eta J_{i,j} \overline{Q}_{i,j}^n \right)
\end{aligned}
\qquad (18)
$$

The $\varepsilon_{i,j}^{(2)}$ and $\varepsilon_{i,j}^{(4)}$ terms are defined as

$$
\begin{aligned}
\varepsilon_{\xi_{i,j}}^{(2)} &= K_2 \Delta t \max \left(\nu_{\xi_{i+1,j}}, \nu_{\xi_{i,j}}, \nu_{\xi_{i-1,j}} \right) \\
\varepsilon_{\xi_{i,j}}^{(4)} &= \max \left[0, \left(K_4 \Delta t - \varepsilon_{\xi_{i,j}}^{(2)} \right) \right] \\
\varepsilon_{\eta_{i,j}}^{(2)} &= K_2 \Delta t \max \left(\nu_{\eta_{i,j+1}}, \nu_{\eta_{i,j}}, \nu_{\eta_{i,j-1}} \right) \\
\varepsilon_{\eta_{i,j}}^{(4)} &= \max \left[0, \left(K_4 \Delta t - \varepsilon_{\eta_{i,j}}^{(2)} \right) \right]
\end{aligned}
\qquad (19)
$$

The coefficients of the second difference dissipation terms, $\nu_{i,j}$, are defined as

$$
\begin{aligned}
\nu_{\xi_{i,j}} &= \frac{|p_{i+1,j} - 2p_{i,j} + p_{i-1,j}|}{(p_{i+1,j} + 2p_{i,j} + p_{i-1,j})} \\
\nu_{\eta_{i,j}} &= \frac{|p_{i,j+1} - 2p_{i,j} + p_{i,j-1}|}{(p_{i,j+1} + 2p_{i,j} + p_{i,j-1})}
\end{aligned}
\qquad (20)
$$

Typical values[5, 6] for the K_2 and K_4 constants are $K_2 = 1/4$ and $K_4 = 1/100$. Tests were also performed by varying these constants in some neighborhood of these suggested values, and the results will be described shortly. The term $\sigma_{i,j}$ is a spectral radius scaling, which can be defined in two dimensions as

$$
\sigma_{i,j} = \left(|U| + a\sqrt{\xi_x^2 + \xi_y^2} + |V| + \sqrt{\eta_x^2 + \eta_y^2} \right)_{i,j} \qquad (21)
$$

We observe that, with the above definition, $\sigma_{i,j}$ is the sum of the spectral radii of the inviscid flux Jacobian matrices $\hat{A}$ and $\hat{B}$.

At points adjacent to the computational boundaries, the fourth order artificial dissipation term used in the constant coefficient model is reduced to a second order term similar to the terms used in the left-hand side operators. Hence,

$$
\left(D_\xi^{(4)} \right)_{\text{boundary}} = -\Delta t \, \varepsilon_E \, J^{-1} \nabla_\xi \Delta_\xi \, J \overline{Q}^n \qquad (22)
$$

with a similar expression for the η-direction. In the nonlinear artificial dissipation case, the operator used at points adjacent to the boundary is obtained simply by setting $\varepsilon_{i,j}^{(4)}$ to zero. As discussed by Pulliam[6], ideally one would like to use in the left-hand side implicit operators the same artificial dissipation operator used in the explicit side. However, in the present context, in order to accomplish this in a computationally efficient way, it would be necessary to implement the so-called diagonal algorithm (see, for instance, Pulliam and Chaussee[18], and Chaussee and Pulliam[19]). Since we did not implement the diagonal algorithm in the present work, we are restricted in the left-hand side operators to the use of second difference artificial dissipation terms in order to avoid spoiling the tridiagonal characteristic of the LHS matrices. The form of the implicit artificial dissipation terms is already shown in Eq. (16). With the constant coefficient model, we used $\varepsilon_I = 3\varepsilon_E$, and with the nonlinear model we used $\varepsilon_I = 3 \left(\varepsilon_{i,j}^{(2)} + \varepsilon_{i,j}^{(4)} \right)$. We further observe that the values of $\varepsilon_{i,j}^{(2)}$ and of $\varepsilon_{i,j}^{(4)}$ are different for operation in the ξ-direction and for operation in the η-direction, as shown in Eqs. (19).

Previous experience with a 2-D transonic nozzle flow problem[8] has shown that the use of a constant time step throughout the flow-field, with the present numerical scheme, yields a rather slow con-

vergence rate. Hence, a spatially variable time step option was implemented in the present work. The idea in this case is to try to maintain a constant CFL number throughout the field. There are several suggestions in the literature on simplified ways of implementing a variable time step option, and the interested reader is referred to the works of Pulliam[4], Pulliam and Steger[5], and Ying[20] for examples of such implementations. Here, however, we have decided to use a different approach which starts directly with the definition of the CFL number as

$$CFL = \frac{c\,\Delta t}{\Delta s} \tag{23}$$

where c is some characteristic speed of propagation of information in the flowfield, and Δs is some characteristic mesh spacing. In the present implementation, we computed $c_{i,j}$ as the maximum characteristic speed associated with either the ξ- or η-directions. Hence,

$$c_{i,j} = \max\left(|U| + a\sqrt{\xi_x^2 + \xi_y^2}\,,\ |V| + a\sqrt{\eta_x^2 + \eta_y^2}\right)_{i,j} \tag{24}$$

Since all of the present implementation is being performed in general curvilinear coordinates, we take $\Delta s = \Delta \xi = \Delta \eta = 1$. Therefore, the local time step at a point (i,j) is given by

$$\Delta t_{i,j} = \frac{CFL}{c_{i,j}} \tag{25}$$

For the cases with variable time stepping, the CFL number must be provided by the user and it is assumed constant throughout the flowfield. The above variable time step convergence acceleration procedure has yielded up to 30 times faster convergence rates than the constant Δt option, in some cases.

The characteristic relations given by Eqs. (8) and (14), which are used for entrance and exit boundary condition implementation in the 2-D and axisymmetric cases, respectively, must also be discretized in a finite difference format. In the present work, these equations are time-marched using the implicit Euler method, and the spatial derivatives are discretized using one-sided, 1st order, finite difference approximations. For instance, if we consider the exit station in the axisymmetric case, the four relations given in Eq. (14) can be written as

$$\delta\rho_{I,j}^n - \left(\frac{1}{a^2}\right)_{I-1,j}^{n+1}\delta p_{I,j}^n = -\left(\frac{\lambda_1}{1+\lambda_1}\right)\left[\left(\rho_{I,j}^n - \rho_{I-1,j}^{n+1}\right)\right.$$
$$\left.-\left(\frac{1}{a^2}\right)_{I-1,j}^{n+1}\left(p_{I,j}^n - p_{I-1,j}^{n+1}\right)\right] \equiv \mathcal{R}_1$$

$$\delta v_{I,j}^n = -\left(\frac{\lambda_1}{1+\lambda_1}\right)\left(v_{I,j}^n - v_{I-1,j}^{n+1}\right) \equiv \mathcal{R}_2 \tag{26}$$

$$\delta p_{I,j}^n + (\rho a)_{I-1,j}^{n+1}\delta u_{I,j}^n = -\left(\frac{\lambda_3}{1+\lambda_3}\right)\left[\left(p_{I,j}^n - p_{I-1,j}^{n+1}\right)\right.$$
$$\left.+(\rho a)_{I-1,j}^{n+1}\left(u_{I,j}^n - u_{I-1,j}^{n+1}\right)\right] - \left(\frac{\Delta t}{1+\lambda_3}\right)\left(\frac{\gamma p v}{R}\right)_{I-1,j}^{n+1} \equiv \mathcal{R}_3$$

$$\delta p_{I,j}^n - (\rho a)_{I-1,j}^{n+1}\delta u_{I,j}^n = -\left(\frac{\lambda_4}{1+\lambda_4}\right)\left[\left(p_{I,j}^n - p_{I-1,j}^{n+1}\right)\right.$$
$$\left.-(\rho a)_{I-1,j}^{n+1}\left(u_{I,j}^n - u_{I-1,j}^{n+1}\right)\right] - \left(\frac{\Delta t}{1+\lambda_4}\right)\left(\frac{\gamma p v}{R}\right)_{I-1,j}^{n+1} \equiv \mathcal{R}_4$$

where $i = I$ represents the exit station, and $\delta(\ )^n = (\ )^{n+1} - (\ )^n$. The λ terms which appear in the above equations are defined as

$$\lambda_1 = \frac{\Delta t\ u_{I-1,j}^{n+1}}{x_{I,j} - x_{I-1,j}} \qquad \lambda_3 = \frac{\Delta t\ (u+a)_{I-1,j}^{n+1}}{x_{I,j} - x_{I-1,j}}$$

$$\lambda_4 = \frac{\Delta t\ (u-a)_{I-1,j}^{n+1}}{x_{I,j} - x_{I-1,j}} \tag{27}$$

As previously discussed, at a subsonic exit p_{exit} is fixed and, hence, $\delta p_{I,j}^n = 0$. Therefore, using the first three equations in the set of Eqs. (26), we can obtain

$$\delta\rho_{I,j}^n = \mathcal{R}_1 \qquad \delta v_{I,j}^n = \mathcal{R}_2 \qquad \delta u_{I,j}^n = \frac{\mathcal{R}_3}{(\rho a)_{I-1,j}^{n+1}} \tag{28}$$

If the exit is supersonic, all four relations should be used, and this yields

$$\delta p_{I,j}^n = \frac{\mathcal{R}_3 + \mathcal{R}_4}{2} \qquad \delta\rho_{I,j}^n = \mathcal{R}_1 + \left(\frac{1}{a^2}\right)_{I-1,j}^{n+1}\delta p_{I,j}^n$$

$$\delta v_{I,j}^n = \mathcal{R}_2 \qquad \delta u_{I,j}^n = \frac{\mathcal{R}_3 - \delta p_{I,j}^n}{(\rho a)_{I-1,j}^{n+1}} \tag{29}$$

From the foregoing expressions, one can determine the conserved variables at the exit boundary for an axisymmetric flow case. Similar expressions could be written for the entrance station in the axisymmetric case, and for both the entrance and exit boundaries in the 2-D case. Finally, we should observe that all boundary conditions were implemented explicitly in the present work, in the sense that no modification of the LHS matrices was performed in order to account for the boundary conditions as previously described.

Grid Generation

All grids used in the present investigation were generated using algebraic schemes. Grid point distribution in the wall-to-centerline direction, η-direction, is controlled using exponential stretching functions. The logic in the grid generation code allows for grid point clustering towards the nozzle wall, or both towards the wall and the centerline. In either case, the grid stretching factor must be specified by the user, and the grid η increments are computed for the throat station. The grid η increments at any other station are computed from the throat increments proportional to the ratio of the local nozzle radius, or nozzle height in the 2-D case, to the throat radius or height. In the entrance-to-exit direction, ξ-direction, the grids also have exponential stretching in order to cluster grid points primarily in the throat region, where one can typically expect larger property gradients. An option that would allow both clustering at the throat and at the exit, for the nozzle divergent section, was also implemented due to the appearance of shock waves in the divergent portion of the nozzle.

With regard to the constant ξ lines, two rather different forms of grid topology were implemented in the present work. In the first one, which we will refer to here as "straight" η-lines, the constant ξ lines are simply generated as vertical lines aligned with the y-axis and spanning the nozzle semi-height, as indicated in Fig. 1. Grids with this topology are easier to generate but they have the drawback that nominally normal lines do not intercept the nozzle wall at $90°$ angles for the convergent and divergent sections. At least in principle, for realistic nozzles with steep convergent and divergent sections, the error introduced by extrapolating pressure and temperature at the wall with a nonorthogonal wall grid should be relevant. Hence, a second grid topology, which we will refer here as having "curved" η-lines, was implemented. An example of such grid is shown in Fig. 2. In this case, the constant ξ lines are generated using quadratic polynomials, in which the point and slope at the wall, and the slope at the centerline, are fixed. This will allow grids which are orthogonal both at the nozzle wall and at the centerline.

For all cases treated in the present work, only the upper, or lower, portion of the nozzle was considered, due to obvious symmetry considerations. However, there are also differences in the meshes generated for 2-D flow calculations and meshes generated for axisymmetric cases.
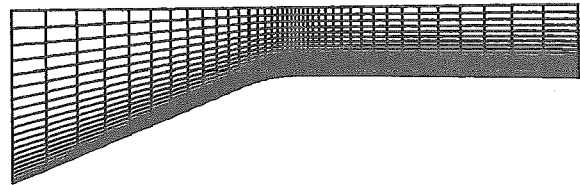
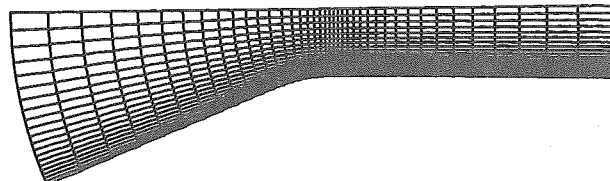

Figure 1: Example of computational mesh with straight η-lines.

Figure 2: Example of computational mesh with curved η-lines.

The former have an extra grid line "on the other side" of the centerline in order to ease the enforcement of boundary conditions. In the latter case, since axisymmetric centerline boundary conditions are enforced by making the normal flux equal to zero, the centerline itself is the boundary.

Two-Dimensional Results

The first set of results that will be considered in the 2-D case has the objective of validating the solution method and of investigating the solution behavior with grid refinement. The nozzle geometry considered in this initial validation phase is the same one used by MacCormack[11], and which has been experimentally investigated by Mason et al.[21]. This is a 2-D transonic convergent-divergent nozzle in which the throat is located half way between the entrance of the convergent section and exit plane. The total length of the nozzle is 0.38 ft (0.116 m), and the throat half-height is 0.045 ft (0.014 m). The wall dimensionless radius of curvature at the throat is 2, referred to the throat half-height, the convergent angle is 22.33°, and the divergent angle is 1.21°. A typical computational mesh used in these numerical studies is shown in Fig. 3. The grid has 49 points in the streamwise direction and 22 points in the wall normal direction. Grid points are clustered towards the wall in the normal direction, and towards the throat in the streamwise direction, through the use of exponential one-dimensional grid stretching functions. This mesh uses the straight η-lines grid topology, previously discussed, and a section with constant crossflow area was added upstream of the convergent section.

The stagnation conditions at the entrance station considered in this analysis are $T_t = 531.2$ °R (294.8 K) and $P_t = 2117.0$ lb/ft^2 (1.0136×10^5 N/m^2). We further set the flow entrance angle to zero. The exit pressure, in the initial condition, is set to $P_t/3$, which guarantees that the flow becomes supersonic in the divergent section for this case and, hence, the exit conditions are completely determined by the flow itself after convergence. A summary of the results obtained in this case is presented in Fig. 4 in terms of the wall pressure distribution, made dimensionless by the entrance stagnation pressure, plotted versus the nozzle axial position nondimensionalized by the length of the divergent section. In this figure, the present computational results are compared to experimental results due to Mason et al.[21] and to computational results due to MacCormack[11] obtained on a comparable mesh. The fine mesh indicated in Fig. 4 is precisely the computational grid shown in Fig. 3. The coarse grid has half the number of grid points in both directions along the convergent and divergent sections of the nozzle. Moreover, it does not have the straight section upstream of the convergent section. These results use a constant dimensionless $\Delta t = 0.01$, and a constant coefficient artificial dissipation model with $\varepsilon_E = 1$. It is clear from Fig. 4 that the present computational results on the finer grid do reproduce well the experimental results of Mason et al.[21], despite the fact that only the inviscid terms are included in the present formulation. In the present investigation, at least 5 to 6 orders of magnitude drop in the maximum residue in the field were required before convergence was accepted. Previous experience[8] has shown that typically a drop of about 3 orders of magnitude in the residue is enough for plotting accuracy.

The wall pressure distribution results presented in Fig. 4 indicate the formation of a shock wave just downstream of the nozzle throat. The mechanism for the formation of this shock is also discussed by Back and Cuffel[22] for an axisymmetric nozzle, and it can be described in terms of an overturning of the flow through the curved throat section. When the flow reaches the straight wall divergent section, this causes a local recompression which can only be accomplished through a shock wave, since the flow is already supersonic. According to the results presented by Back and Cuffel[22], this oblique shock
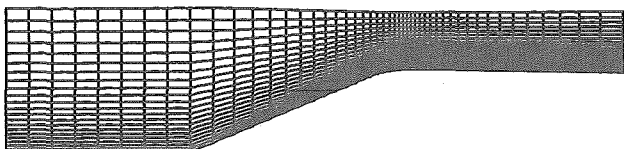
should extend all the way to the nozzle centerline. Despite the fact that we have here a 2-D flow situation, there is no reason to believe that this should not be the case here too. Fig. 5 presents the pressure distributions along the nozzle centerline for three different grid sizes. It is clear from this figure that the coarsest mesh result does not present the evidence of any shocks. Moreover, a pressure rise just downstream of the throat can be observed for the finer meshes, but this is very much attenuated in comparison with the corresponding pressure rise at the wall. This has prompted the question of whether the amount of artificial dissipation being used was excessive and, hence, it was damping truly physical property gradients in the field.

In order to investigate this possibility, the problem was solved using the fine mesh shown in Fig. 3 and various values of the artificial dissipation coefficient ε_E. The linear constant coefficient artificial dissipation model was employed for this investigation. Dimensionless pressure distribution along the nozzle wall and along the nozzle centerline are shown in Figs. 6 and 7, respectively. It is clear from these figures that at least the first shock-shock reflection at the centerline is captured by the solution with small values of ε_E. For the higher values of ε_E, even the original wall shock is smoothed by the excessive artificial dissipation. For the value of ε_E typically recommended in the literature, i.e., $\varepsilon_E \cong 1$, Fig. 5 indicates that there is already too much artificial dissipation in the solution, since the centerline shock is being smoothed out. It is evidenced by Figs. 6 and 7 that the first centerline shock reflection is much better captured by the scheme with $\varepsilon_E = 0.5$. Moreover, even the first shock reflection at the wall is captured by the solution with $\varepsilon_E = 0.5$, whereas this feature is not present in the other results. For $\varepsilon_E = 2.0$, we notice an appreciable attenuation of
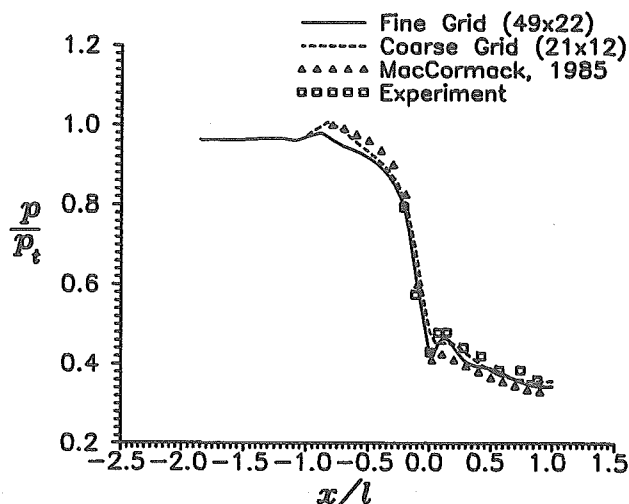
Figure 4: Summary of initial 2-D validation results and grid refinement study.
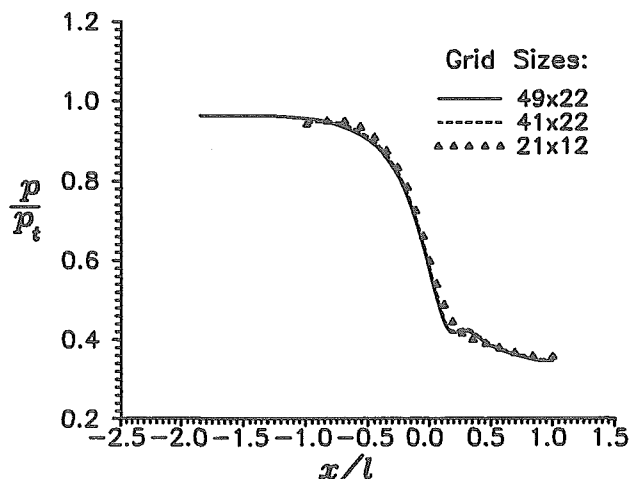
Figure 5: Centerline pressure distribution for 2-D convergent-divergent nozzle.

Figure 3: Nozzle geometry and fine mesh for initial 2-D code validation runs.

the wall shock, and the centerline shock has almost completely disappeared. For values of ε_E smaller than 0.5, i.e., of the order 0.1 to 0.2, the code diverges in this case.

The effect of mesh topology in the results, i.e., whether nominally normal lines are truly orthogonal to the wall, or not, was investigated. The meshes used in this study are precisely the ones shown in Figs. 1 and 2. The solutions are compared in terms of wall pressure distributions in Fig. 8. In this case, a constant coefficient artificial dissipation model was used with $\varepsilon_E = 1.0$. Fig. 8 shows that there is not much difference between the two results. It is clear that both grids have a rather good clustering of grid points towards the wall, at least for an inviscid computation, which justifies the good agreement between the results despite the locally large differences in the grid near the wall. Moreover, for nozzles with much steeper convergent and/or divergent sections, it is not very realistic to try to use the straight η-lines grid topology and these cases were not run. Nevertheless, the above results show that, even for a 22.33° convergent section, the effect of grid non-orthogonality at the wall can hardly be noticed to plotting accuracy.

In an attempt to establish the robustness of the present method to more demanding 2-D nozzle geometries, the flow through a convergent-divergent nozzle with steeper convergent and divergent sections was investigated. The particular geometry investigated has a 45° convergent section and a 15° divergent section, and various values of dimensionless wall radius of curvature at the throat (R_{wall}) were considered. A typical computational mesh for this investigation is shown in Fig. 9, in which the case of a nozzle with $R_{wall} = 0.625$, nondimensionalized
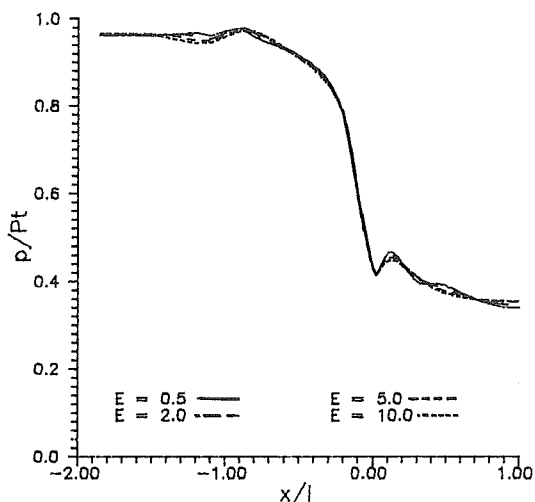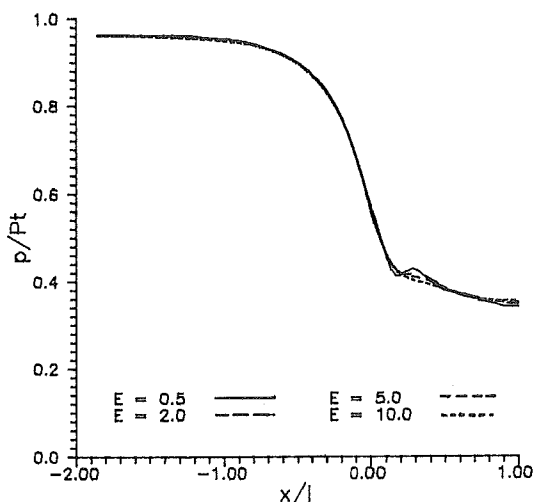
by the throat semi-height, is considered. The meshes used in this case have the curved η-lines grid topology. The grid shown in Fig. 9 has 41 × 22 points in the streamwise and normal directions, respectively. The nozzle exit pressure was set low enough such that the flow would be supersonic at the exit after convergence. The values of dimensionless wall radius of curvature at the throat considered were 2, 1.5, 1 and 0.625. It is clear that a smaller R_{wall} poses a more stringent test to the formulation. This has manifested itself in the present simulations by requiring larger values of artificial dissipation coefficients to maintain numerical stability for the smaller values of throat radii. A constant coefficient artificial dissipation model was again employed in this investigation. Wall and centerline pressure distributions for the cases of $R_{wall} = 2$ and $R_{wall} = 0.625$ are shown in Fig. 10. Fig. 11 presents contours of constant dimensionless pressure for the case of $R_{wall} = 0.625$. Despite the fact that larger values of artificial dissipation coefficients are used for the cases with tighter throat radii, it is clear from Fig. 10 that a stronger shock is formed in the case of smaller radius, and that the expansion through the throat is also faster in this case. Moreover, the observation that nozzles with tighter wall radius of curvature at the throat do require larger amounts of artificial dissipation had been previously reported by Silva[23]. In that case, it was found that an explicit, upwind, MacCormack-type scheme needed some explicitly added artificial dissipation in order to maintain stability for the solution of the flow through an axisymmetric nozzle with longitudinal cross-section much similar to the one shown in Fig. 9. Here, the same sort of behavior is being observed for a centered Beam and Warming-type scheme.

Another important point to be considered is the effect of the numerical boundary condition schemes used in the present implementation. The first aspect studied deals with the pressure boundary condition at a wall. As discussed by MacCormack[7], in the inviscid flow case, the zero normal pressure gradient boundary condition is only strictly correct if the wall is flat. For curved walls, a centrifugal-type acceleration term must be taken into account in order to determine the pressure at the wall. In order to make sure that no other effect would be influencing the results of this study, the computational meshes used in the present investigation have the curved η-lines grid topology, which guarantees grid orthogonality at the wall. The same nozzle geometries discussed in the previous paragraph were used in this study. It is clear that, the tighter the wall radius of curvature, the more pronounced the centrifugal acceleration effect should be (see, for instance, Eq. (9)). The present computational results have indeed shown this feature and, for the cases with $R_{wall} = 2$ and $R_{wall} = 1.5$, the effect of the centrifugal acceleration term is completely negligible[24]. For the cases with $R_{wall} = 1$ and $R_{wall} = 0.625$, the effect is still small but one can see some differences in the wall pressure distribution, especially for the case with the smallest radius. The comparison of the results, in terms of pressure distribution at the wall, with and without centrifugal term correction for the case with $R_{wall} = 0.625$, is shown in Fig. 12. A comparison of the same results in terms of wall Mach number is shown in Fig. 13. It is clear that, even for this case with the smallest throat radius, the effect of the correction is indeed

Figure 6: Effect of artificial dissipation coefficient on the 2-D nozzle wall pressure distribution.

Figure 7: Effect of artificial dissipation coefficient on the 2-D nozzle centerline pressure distribution.
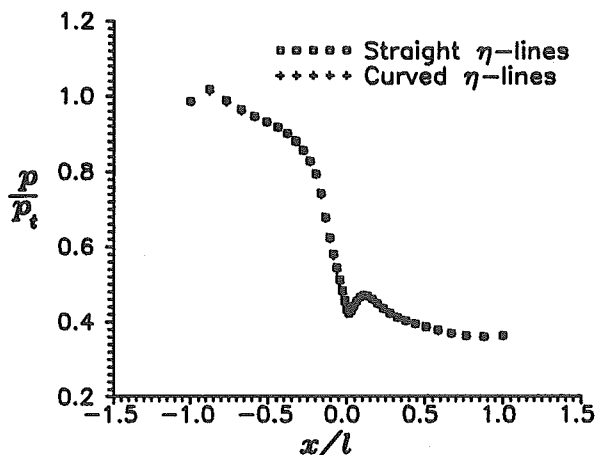

Figure 8: Effect of the wall grid orthogonality in the 2-D transonic nozzle results.

very small. Moreover, the major significance of the possible effect of the present difference in boundary condition implementation would be in the position of the transonic nozzle sonic line. However, Fig. 13 makes it evident that the position of the sonic line is not affected at all by the difference in the wall pressure boundary condition implementation, not even in the worst case. Therefore, although it would be worth implementing the curved wall-type boundary condition because it is more correct and it does not cause any increase in computational time, at least for the cases analyzed here it would not significantly increase the accuracy of the results.

The effect of "weak" versus "strong" boundary condition enforcement at the nozzle centerline was also subject of investigation in the 2-D case. The major purpose of this study was a preparation for the analysis of axisymmetric cases. In 2-D, both forms of centerline boundary condition enforcement can be conveniently, and accurately, implemented. This is not so in the axisymmetric case due to the transformation singularity that exists at the centerline. Hence, it is most desirable to use a weak boundary condition enforcement in the axisymmetric case. Therefore, the objective here was to evaluate the effect of using the centerline boundary condition implemented in a weak fashion for the 2-D case, in comparison with all the previous results already available. The nozzle geometry and grid shown in Fig. 3 were used for this investigation. It was observed that the difference in the form of boundary condition implementation did not change either the converged results or the convergence rate. Convergence history
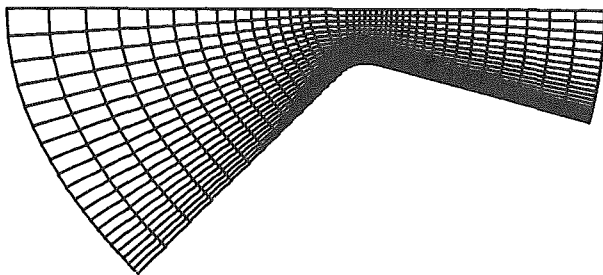
Figure 9: Typical computational mesh for study of the wall radius of curvature at the throat effect (in this case, $R_{\text{wall}} = 0.625$).
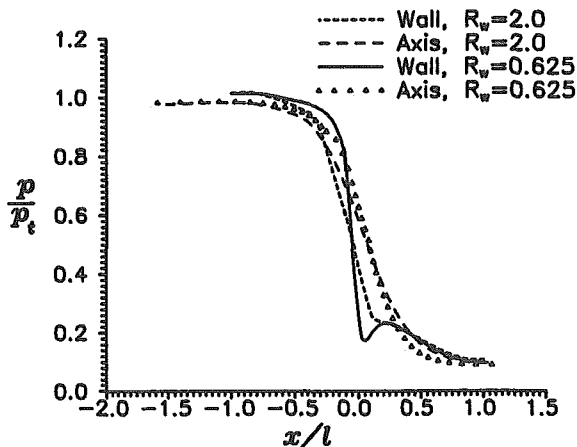

Figure 10: Effect of wall radius of curvature at the throat on nozzle flow solution.
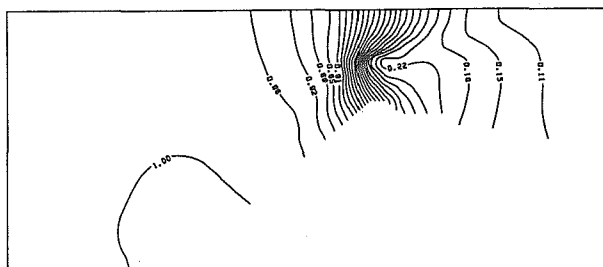

Figure 11: Pressure contours for nozzle with dimensionless wall radius of curvature at the throat equal to 0.625.

plots for the two cases are shown in Fig. 14. The highly oscillatory residue plot for the strong boundary condition case, for very low values of maximum residue, are believed to be related to the low accuracy of the equipment in which this simulation was run and are not related to the form of boundary condition implementation itself. These results provided confidence that implementing the centerline boundary condition in a weak fashion for the axisymmetric case would not cause any problems.

Axisymmetric Results

Initially, the solution of an axisymmetric nozzle flow was attempted using the same constant coefficient artificial dissipation model which was used in the 2-D computations. However, it was found that the axisymmetric solutions behave in quite a different way with regard to the values of the constant artificial dissipation coefficient ε_E. Whereas an increase in ε_E would always increase the stability of the scheme in 2-D, obviously at the expense of spatial resolution, the same was not true for the axisymmetric case. It was observed, in the axisymmetric case, that there existed an optimum value of ε_E for which the solution is stable and the spatial resolution is good. If we decrease ε_E from this value, initially a degradation of the spatial resolution occurs, and eventually the solution becomes unstable as ε_E tends to zero. Increasing ε_E from its optimum value, we notice that the numerical solution tends to become more oscillatory. Initially, these oscillatory solutions are stable, fully converged solutions. As we keep increasing ε_E, however, the numerical solutions again become unstable. Moreover, it was observed that this optimum value of ε_E is almost one order of magnitude smaller than the corresponding best value of this coefficient that should be used in a 2-D nozzle problem with the same convergent and
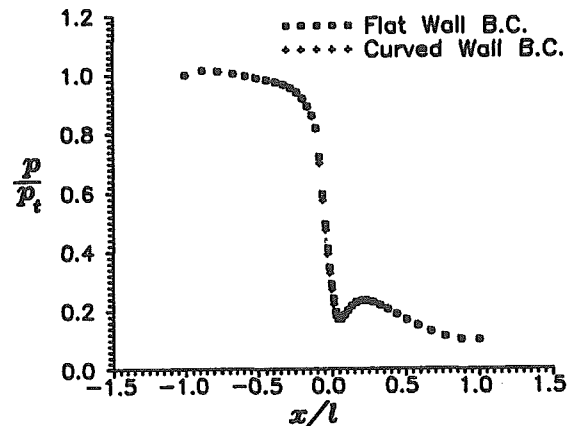

Figure 12: Effect of centrifugal term correction on wall pressure boundary condition for nozzle with $R_{\text{wall}} = 0.625$. Wall pressure distribution.
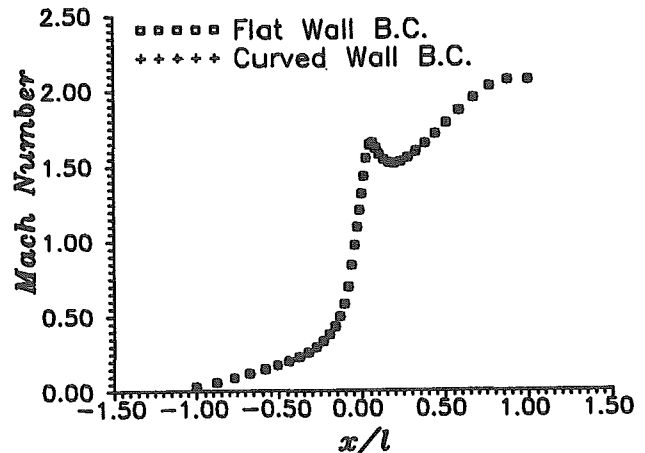

Figure 13: Effect of centrifugal term correction on wall pressure boundary condition for nozzle with $R_{\text{wall}} = 0.625$. Wall Mach number distribution.

divergent angles, and the same R_{wall} at the throat.

Some of the results obtained in this investigation are shown in Figs. 15 and 16. Fig. 15 presents the wall pressure distributions whereas Fig. 16 has the centerline pressure distributions. The nozzle geometry and computational grid used in this investigation are the axisymmetric counterpart of what is shown in Fig. 3. The behavior previously described can be clearly seen in the various curves shown in Figs. 15 and 16. It was found that, in this case, the best value of the constant artificial dissipation coefficient was around $\varepsilon_E = 0.075$. The corresponding convergence histories for some of these solutions are shown in Fig. 17. We observe that the case with $\varepsilon_E = 0.050$ seems to be close to a lower bound in the value of the artificial dissipation coefficient for stability. From Fig. 17, we can see that the solution is apparently converging until about 11000 iterations, when it starts to slowly diverge. It is interesting, however, that the pressure distributions at the wall and centerline for this case, after the 16000 iterations for which this simulation was run, seem to be quite reasonable, as one can see from Figs. 15 and 16. On the other hand, the pressure distributions for the case with $\varepsilon_E = 0.750$ are highly oscillatory and unrealistic, but the convergence process is stable. Simulations with $\varepsilon_E = 1$ were also performed for this configuration and the numerical solution process is stable, but the pressure distributions look even worse than those for the case $\varepsilon_E = 0.750$. Further increase in ε_E, however, makes the solution unstable. Nevertheless, a situation, as here described, in which an increase in the amount of artificial dissipation in the solution produces the opposite effect of what was intended, is not acceptable.

It seems to us that the oscillations that appear in the solutions with larger values of ε_E are due to the natural tendency of the fourth difference dissipation terms of producing oscillations every time the scheme sees steep property gradients (see, for instance, Pulliam[6] for a discussion of this point). Somehow, this tendency seems to be exaggerated in the axisymmetric case, and it is destroying the corresponding numerical solutions. The remedy employed here was to implement the nonlinear artificial dissipation model[6], which uses a blend of second and fourth difference terms, and in which the fourth difference terms are automatically turned off, as previously described, everywhere there are strong pressure gradients. A comparison of the solution obtained with the nonlinear artificial dissipation model for the same geometry is presented in Fig. 18, in which the best result with a constant ε_E, i.e., $\varepsilon_E = 0.075$, is also shown. Both wall and centerline pressure distributions are shown in this figure. For the nonlinear artificial dissipation model, the parameters K_2 and K_4 were set to the values 0.125 and 0.01, respectively, in this simulation. We observe that this value of K_2 is about half of what is typically recommended in the literature[5, 6]. As a general rule, we also noticed that smaller values of these parameters, as compared to what is typically recommended, tend to produce better results. However, for the nonlinear artificial dissipation model, the behavior of the solution process seems to be less sensitive to the values of these constants than the situation previously described for the linear constant coefficient model.

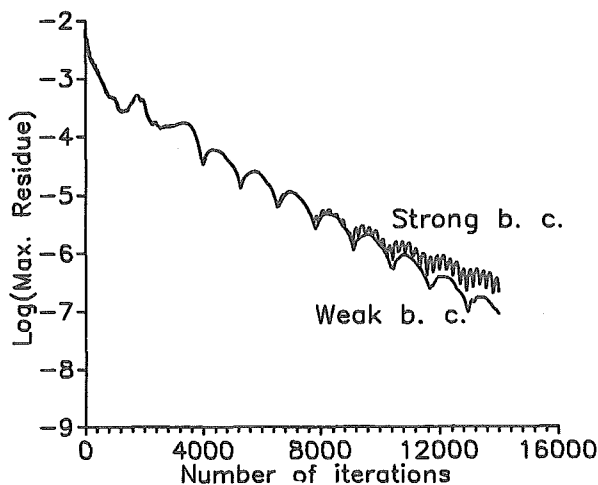A feature which was extensively tested with the present axisym-

metric version of the code refers to convergence acceleration through the use of spatially varying time steps. As previously described, the implementation adopted here tries to guarantee a constant CFL number throughout the field. The convergence history results shown in Fig. 19 are indicative of the increase in convergence rate which is achieved through the use of variable time stepping. In this case, the variable Δt solution used a CFL number of 10. The nozzle geometry used for these tests is the axisymmetric version of the one shown in Fig. 3. As in all previous tests, the exit pressure was set low enough in order to provide supersonic flow throughout the nozzle divergent section. It is interesting to observe that, after a few iterations, the
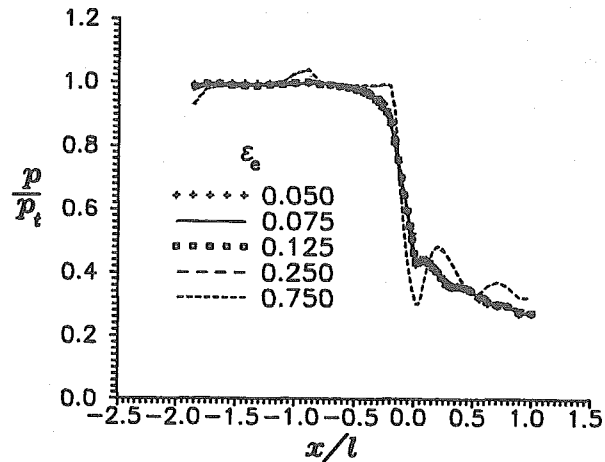

Figure 15: Effect of the constant artificial dissipation coefficient in the wall pressure distribution for an axisymmetric nozzle.
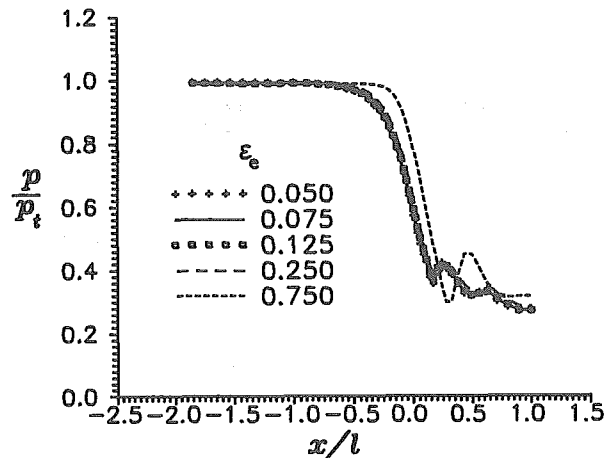

Figure 16: Effect of the constant artificial dissipation coefficient in the centerline pressure distribution for an axisymmetric nozzle.

Figure 14: Comparison of centerline boundary condition effect on solution convergence rate.
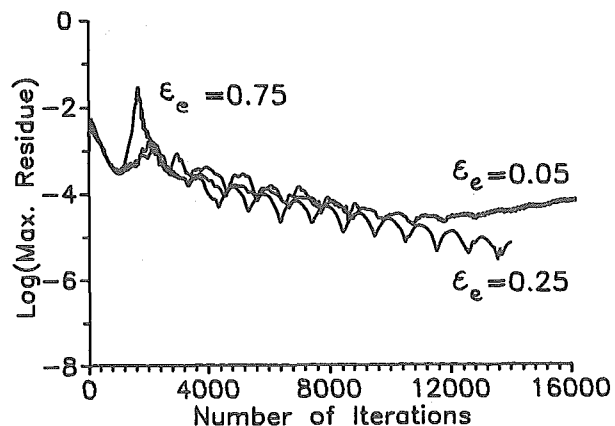

Figure 17: Effect of the constant artificial dissipation coefficient in the convergence history for some axisymmetric nozzle flow simulations.

maximum residue drop is essentially monotonic for the case with constant CFL (variable Δt). On the other hand, all cases run with the constant Δt option exhibit some sort of oscillation in the maximum residue as iterations progress. This observation is also corroborated by previous 2-D nozzle flow simulations[8].

Despite the fact that a linear stability analysis would indicate that the 2-D, or axisymmetric, Beam and Warming algorithm is unconditionally stable, it is well known that this is not the case in practice. In other words, attempts to run the algorithm at extremely large CFL numbers will lead to numerical instability or, at the best, very slow convergence. Using again the axisymmetric counterpart of the nozzle geometry shown in Fig. 3, we performed a study of the value of CFL which would yield the fastest convergence rate. A summary of the convergence rate results obtained in this case is presented in Fig. 20. It can be seen from the figure that the fastest convergence rate is obtained for $CFL = 5$ in this case. A $CFL = 1$ yields essentially the same convergence rate as a $CFL = 10$. Moreover, for the cases with a CFL number larger than 10, a "soft start" procedure had to be implemented because the code would diverge if, for instance, we would attempt to run it from the stagnation condition already with $CFL = 50$. For this $CFL = 50$ case, for example, this soft start was implemented by running 10 iterations with $CFL = 10$, then another 10 iterations with $CFL = 20$, and finally letting the code converge with $CFL = 50$. Nevertheless, the asymptotic convergence rate, i.e., after these few initial iterations, is well defined for all cases, and the fastest convergence is obtained with $CFL = 5$, as previously discussed. For all of these cases, the spatially variable Δt was computed according to Eq. (25), and the nonlinear artificial dissipation model was used with $K_2 = 0.125$ and $K_4 = 0.01$.

Studies of the effect of grid orthogonality at the wall, of the cen-
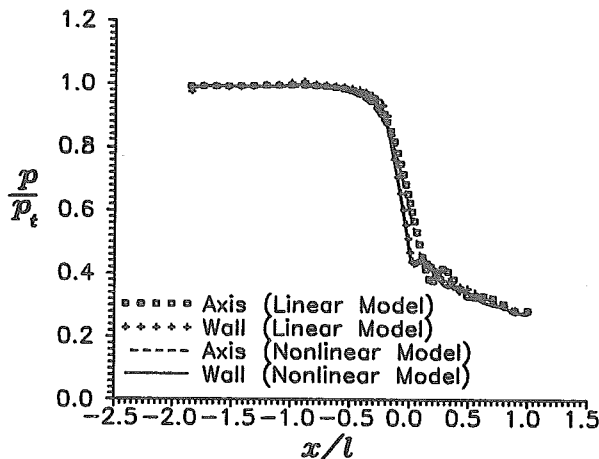
trifugal acceleration correction on the wall pressure boundary condition, and of the wall radius of curvature at the throat were also performed for the axisymmetric case. However, the conclusions which can be drawn from this investigation are essentially similar to the ones obtained in the corresponding 2-D studies. Therefore, we will not present these results here in the interest of brevity. The studies of convergence rate, whose results are summarized in Fig. 20, have also pointed out that the slowest computational points to converge are typically at the nozzle exit boundary, regardless of the CFL number used. Therefore, an investigation of the influence of the present form of boundary condition implementation was performed. The comparison was made between solutions using zero-th order extrapolation at entrance and exit boundaries and solutions using the characteristic relations to determine the boundary properties which depend on interior information. The axisymmetric nozzle configuration corresponding to the one shown in Fig. 3 was again used for this study. It was observed that the converged solutions essentially did not change, regardless of the form of boundary condition implementation. The use of zero-th order extrapolation at entrance and exit boundaries, however, has made the convergence rate slightly slower. For example, Fig. 21 compares the convergence histories for the case with a constant $CFL = 10$, and the nonlinear artificial dissipation model with $K_2 = 0.125$ and $K_4 = 0.01$.

The consideration of realistic axisymmetric nozzle geometries was performed by computationally reproducing the experimental results of Back and Cuffel[22]. More information on this experimental effort of measuring pressure distributions on axisymmetric nozzles can be found in Back et al.[25] and Cuffel et al.[26]. The particular configuration considered has a 45° convergent section, a 15° divergent section and a circular-arc throat with dimensionless wall radius of curvature $R_{wall} = 0.625$. R_{wall} is nondimensionalized by the nozzle throat radius. More details of the geometric definitions of this nozzle can

Figure 18: Effect of type of artificial dissipation model on the pressure distribution at the wall and centerline.

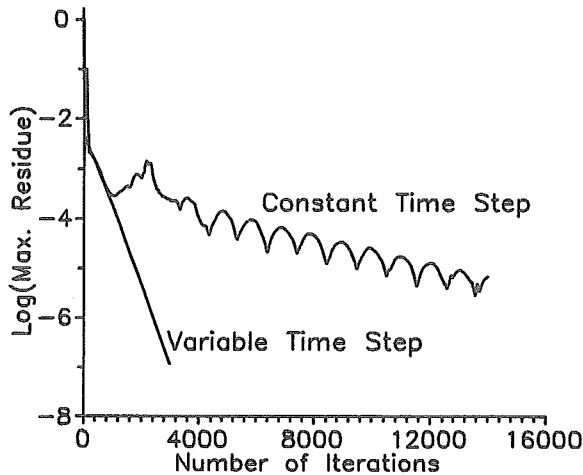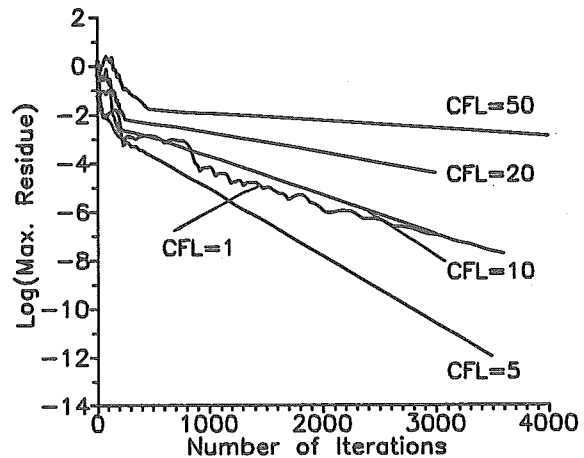Figure 20: CFL number influence on the convergence rate.

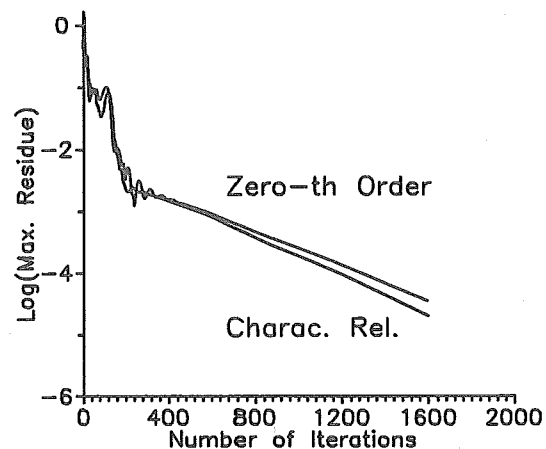Figure 19: Convergence acceleration through the use of variable time stepping.

Figure 21: Effect of entrance and exit boundary condition implementation on the convergence rate.

105

be found in Back and Cuffel[22]. A typical computational grid used in this investigation is shown in Fig. 22. This particular grid has 80 points in the longitudinal direction and 29 points in the crossflow direction. The ratio of specific heats, γ, was taken as 1.35 for this particular study[22], instead of the usual value of 1.4 typically used for air. The nozzle exit pressure was set low enough in order to have fully supersonic flow in the divergent section. A comparison of the present results with those of Back and Cuffel[22] is presented in Fig. 23. Computational results for a 50 × 25 mesh and for a 80 × 29 mesh are presented. These simulations were run with a CFL number of 2, and using $K_2 = 0.1$ and $K_4 = 0.005$ for the nonlinear artificial dissipation model. For the coarse grid, 5 orders of magnitude drop in the residue were achieved in approximately 600 iterations. About 9 orders of magnitude reduction in the residue were obtained for the fine grid in 2000 iterations. The agreement between the present computational results, for both coarse and fine grids, and the experiment is quite good. Moreover, except for the region immediately upstream of the throat, the two computational results are essentially identical. We observe that the computations do capture the wall shock right downstream of the throat correctly. The shock-shock reflection at the centerline, which is much further downstream in this case, is somewhat smeared in the present computations. This can be attributed to the rather coarse grid in the region where the oblique divergent shock reaches the nozzle centerline. The authors have attempted a local grid refinement, on both the streamwise and crossflow directions, towards the nozzle exit and towards the centerline. However, at least with the structured grids being used here, this invariably causes further grid refinement at the wall near the nozzle exit, and we were unable to obtain a numerically stable solution for this new grid. Back et al.[25], and Back and Cuffel[22] report that flow separation was observed at the wall near the exit station for this nozzle. Therefore, although the subject is still being investigated, at present we believe that there is more physics going on in this region than we can simulate with the present inviscid formulation. Hence, as we refine the mesh towards the exit, and near the wall, numerical instability results.

Finally, the present computational results for the coarse mesh are compared to the computational results of Marchi et al.[27], for the same nozzle, in Fig. 24. The calculations of Marchi et al.[27] use a segregated finite volume formulation, and the results shown in Fig. 24 use a mesh with 1440 × 20 volumes in the streamwise and crossflow directions, respectively. In general terms, we can observe from this figure that a comparable resolution of spatial gradients is achieved with the present method with much fewer grid points. In particular, with regard to the resolution of the wall shock just downstream of the throat, we can see from Fig. 24 that the present algorithm is doing a better job.

Concluding Remarks

Two-dimensional and axisymmetric inviscid, transonic convergent-divergent nozzle flowfields were simulated using a central difference, implicit, approximate factorization algorithm. Nonlinear artificial dissipation terms which employ a blend of second and fourth difference operators were added to the right-hand side Euler terms. Convergence acceleration to steady state was achieved through the use of spatially variable time stepping which attempts to maintain a constant CFL number throughout the flowfield. The algorithm proved to be very robust, and the solution on rather realistic nozzle configurations was obtained. The algorithm, with the variable time stepping option, also proved to be very computationally efficient.

The effects of several parameters were investigated. Among these, the influence of the wall longitudinal curvature for the axisymmetric
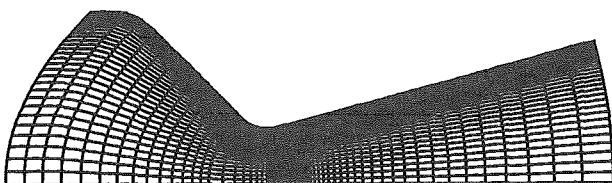
case was shown to be less significant than previously anticipated[24]. A procedure for the implementation of entrance and exit boundary conditions, for the axisymmetric case, based on one-dimensional characteristic relations was developed. Although the concept of characteristics is of fundamental importance in order to determine which conditions should be fixed at a boundary and which conditions should be extrapolated from interior information, it seems that the use of the characteristic relations themselves for this extrapolation process does not yield much more accuracy than simple zero-th order extrapolation in the present case. It was further determined that there exists a range of CFL numbers for which the convergence is faster. Increase of the CFL number above this range will actually slow down convergence, instead of speeding it up.
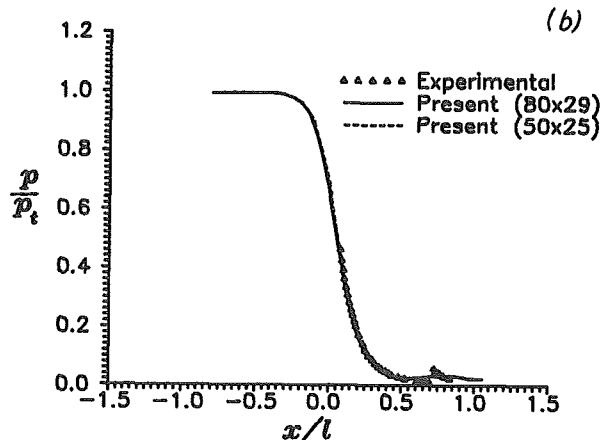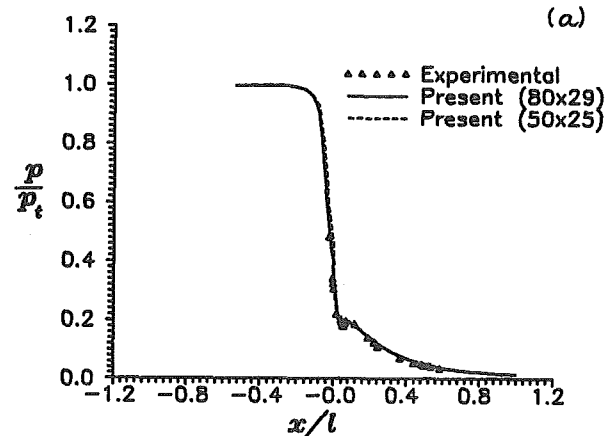

Figure 23: Axisymmetric computation-to-experiment validation and grid refinement study: (a) wall pressures; (b) centerline pressures.

Figure 22: Computational mesh and nozzle geometry for realistic axisymmetric nozzle computations.
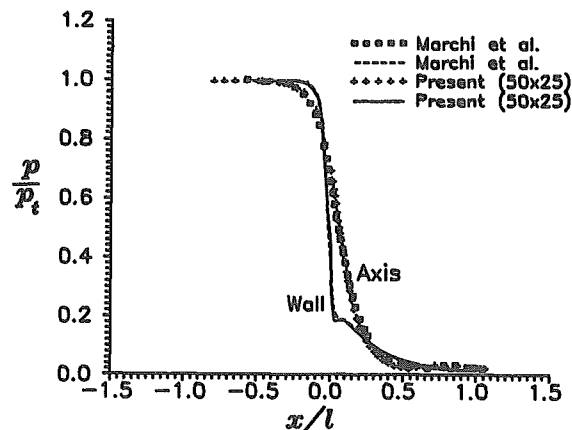

Figure 24: Computation-to-computation comparison of axisymmetric results.

Numerical stability problems were observed with very fine grids near the exit station for nozzles with a very long divergent section. At present, these problems are being attributed to the fact that the flow could be separated in this region for the actual nozzle, which is corroborated by experimental evidence[22, 25]. The present formulation does not include this type of phenomenon. Aside from these problems, however, the present simulations have shown very good agreement with the available data. The authors believe that the next logical step as a continuation of the present effort should be directed towards the implementation of viscous terms.

References

[1] Beam, R.M., and Warming, R.F., "An Implicit Finite-Difference Algorithm for Hyperbolic Systems in Conservation-Law Form," *Journal of Computational Physics*, Vol. 22, Sept. 1976, pp. 87-110.

[2] Beam, R.M., and Warming, R.F., "An Implicit Factored Scheme for the Compressible Navier-Stokes Equations," *AIAA Journal*, Vol. 16, No. 4, April 1978, pp. 393-402.

[3] Pulliam, T.H., and Steger, J.L., "Implicit Finite-Difference Simulations of Three-Dimensional Compressible Flow," *AIAA Journal*, Vol. 18, No. 2, Feb. 1980, pp. 159-167.

[4] Pulliam, T.H., "Euler and Thin Layer Navier-Stokes Codes: ARC2D, ARC3D," Notes for *Computational Fluid Dynamics User's Workshop*, The University of Tennessee Space Institute, Tullahoma, Tenn. , March 12-16, 1984.

[5] Pulliam, T.H., and Steger, J.L., "Recent Improvements in Efficiency, Accuracy and Convergence for Implicit Approximate Factorization Algorithms," AIAA Paper 85-0360, AIAA 23rd Aerospace Sciences Meeting, Reno, Nevada, Jan. 1985.

[6] Pulliam, T.H., "Artificial Dissipation Models for the Euler Equations," *AIAA Journal*, Vol. 24, No. 12, Dec. 1986, pp. 1931-1940.

[7] MacCormack, R.W., "An Introduction and Review of the Basics of Computational Fluid Dynamics," AIAA Professional Study Series on Computational Fluid Dynamics, Snowmass, Colorado, June 1984.

[8] Azevedo, J.L.F., "Euler Solutions of Transonic Nozzle Flows," *Proceedings of the 3rd Brazilian Thermal Sciences Meeting*, Vol. I, Itapema, SC, Brazil, Dec. 1990, pp. 243-248.

[9] Warming, R.F., Beam, R.M., and Hyett, B.J., "Diagonalization and Simultaneous Symmetrization of the Gas-Dynamic Matrices," *Math. Comp.* , Vol. 29, No. 132, Oct. 1975, pp. 1037-1045.

[10] Roe, P.L., "Characteristic-Based Schemes for the Euler Equations," *Annual Review of Fluid Mechanics*, Vol. 18, 1986, pp. 337-365.

[11] MacCormack, R.W., "Current Status of Numerical Solutions of the Navier-Stokes Equations," AIAA Paper 85-0032, AIAA 23rd Aerospace Sciences Meeting, Reno, Nevada, January 14-17, 1985.

[12] Mavriplis, D.J., "Accurate Multigrid Solution of the Euler Equations on Unstructured and Adaptive Meshes," *AIAA Journal*, Vol. 28, No. 2, Feb. 1990, pp. 213-221.

[13] Nietubicz, C.J., Pulliam, T.H., and Steger, J.L., "Numerical Solution of the Azimuthal-Invariant Thin-Layer Navier-Stokes Equations," AIAA Paper 79-0010, 17th Aerospace Sciences Meeting, New Orleans, LA, Jan. 1979.

[14] Zdravistch, F., and Azevedo, J.L.F., "Simulation of the Interference Region on a Multibody Satellite Launcher," *Proceedings of the 11th ABCM Mechanical Engineering Conference*, São Paulo, SP, Brazil, Dec. 1991.

[15] Zdravistch, F., "Aerodynamic Flow Simulation Over Cluster Type Configurations," Master Dissertation, Instituto Tecnológico de Aeronáutica, São José dos Campos, SP, Brazil, Nov. 1990 (in Portuguese, original title is "Simulação de Escoamentos Aerodinâmicos em Configurações Tipo Cluster").

[16] Zdravistch, F., and Azevedo, J.L.F., "Numerical Simulation of High Speed Flows Over Complex Satellite Launchers," *Proceedings of the 3rd Brazilian Thermal Sciences Meeting*, Vol. I, Itapema, SC, Brazil, Dec. 1990, pp. 233-238.

[17] Jameson, A., Schmidt, W., and Turkel, E., "Numerical Solution of the Euler Equations by Finite Volume Methods Using Runge-Kutta Time-Stepping Schemes," AIAA Paper 81-1259, AIAA 14th Fluid and Plasma Dynamics Conference, Palo Alto, CA, June 1981.

[18] Pulliam, T.H., and Chaussee, D.S., "A Diagonal Form of an Implicit Approximate-Factorization Algorithm," *Journal of Computational Physics*, Vol. 39, 1981, pp. 347-363.

[19] Chaussee, D.S., and Pulliam, T.H., "Two-Dimensional Inlet Simulation Using a Diagonal Implicit Algorithm," *AIAA Journal*, Vol. 19, No. 2, Feb. 1981, pp. 153-159.

[20] Ying, S.X., "Three-Dimensional Implicit Approximately Factored Schemes for the Equations of Gasdynamics," Ph.D. Dissertation, Dept. of Aeronautics and Astronautics, Stanford University, Report SUDAAR 557, Stanford, CA, June 1986.

[21] Mason, M.L., Putnam, L.E., and Re, R.J., "The Effect of Throat Contouring on Two-Dimensional Converging-Diverging Nozzles at Sonic Conditions," NASA Technical Paper 1704, 1980.

[22] Back, L.H., and Cuffel, R.F., "Detection of Oblique Shocks in a Conical Nozzle with a Circular-Arc Throat," *AIAA Journal*, Vol. 4, No. 12, Dec. 1966, pp. 2219-2221.

[23] Silva, L.F.F., "Evaluation of the Transonic Region in Convergent-Divergent Nozzles," Master Dissertation, Instituto Tecnológico de Aeronáutica, São José dos Campos, Brazil, Oct. 1989 (in Portuguese, original title is "Avaliação da Região Transônica em Bocais Convergente-Divergente").

[24] Ortega, M.A., and Azevedo, J.L.F., "Checking the Influence of Longitudinal Wall Curvature in the Implementation of Boundary Conditions at the Wall of a Convergent-Divergent Nozzle," *Proceedings of the 11th ABCM Mechanical Engineering Conference*, São Paulo, SP, Brazil, Dec. 1991.

[25] Back, L.H., Massier, P.F., and Gier, H.L., "Comparison of Measured and Predicted Flows Through Conical Supersonic Nozzles, with Emphasis on the Transonic Region," *AIAA Journal*, Vol. 3, No. 9, Sept. 1965, pp. 1606-1614.

[26] Cuffel, R.F., Back, L.H., and Massier, P.F., "Transonic Flowfield in a Supersonic Nozzle with Small Throat Radius of Curvature," *AIAA Journal*, Vol. 7, No. 7, July 1969, pp. 1364-1366.

[27] Marchi, C.H., Silva, A.F.C., and Maliska, C.R., "Numerical Solution of Inviscid Flows without Separation of Compressible Fluids in Nozzles," Paper submitted to the 4th Workshop on Combustion and Propulsion, Santos, SP, Brazil, Dec. 1991 (in Portuguese, original title is "Solução Numérica de Escoamentos Inviscidos sem Separação de Fluidos Compressíveis em Tubeiras"; to the authors' knowledge, this work is still unpublished since the workshop was later cancelled).